remote sensing

MDPI

Article

Satellite Monitoring the Spatial-Temporal Dynamics of Desertification in Response to Climate Change and Human Activities across the Ordos Plateau, China

Qiang Guo [1,2], Bihong Fu [1,*], Pilong Shi [1], Thomas Cudahy [3], Jing Zhang [1] and Huan Xu [1,2]

[1] Institute of Remote Sensing and Digital Earth, Chinese Academy of Sciences, Beijing 100094, China; guoqiang@radi.ac.cn (Q.G.); shipl@radi.ac.cn (P.S.); zhangjing2015@radi.ac.cn (J.Z.); xuhuan@radi.ac.cn (H.X.)

[2] University of Chinese Academy of Sciences, Beijing 100049, China

[3] CSIRO Mineral Resources, Australian Resources Research Centre, 26 Dick Perry Avenue, Kensington, Western Australia 6151, Australia; thomas.cudahy@c3dmm.com

* Correspondence: fubh@radi.ac.cn; Tel.: +86-010-8217-8096

Academic Editors: Rasmus Fensholt, Parth Sarathi Roy and Prasad S. Thenkabail
Received: 9 April 2017; Accepted: 21 May 2017; Published: 25 May 2017

Abstract: The Ordos Plateau, a typical semi-arid area in northern China, has experienced severe wind erosion events that have stripped the agriculturally important finer fraction of the topsoil and caused dust events that often impact the air quality in northern China and the surrounding regions. Both climate change and human activities have been considered key factors in the desertification process. This study used multi-spectral Landsat Thematic Mapper (TM), Enhanced Thematic Mapper Plus (ETM+) and Operational Land Imager (OLI) remote sensing data collected in 2000, 2006, 2010 and 2015 to generate a temporal series of the modified soil-adjusted vegetation index (MSAVI), bare soil index (BSI) and albedo products in the Ordos Plateau. Based on these satellite products and the decision tree method, we quantitatively assessed the desertification status over the past 15 years since 2000. Furthermore, a quantitative method was used to assess the roles of driving forces in desertification dynamics using net primary productivity (NPP) as a commensurable indicator. The results showed that the area of non-desertification land increased from 6647 km^2 in 2000 to 15,961 km^2 in 2015, while the area of severe desertification land decreased from 16,161 km^2 in 2000 to 8,331 km^2 in 2015. During the period 2006–2015, the effect of human activities, especially the ecological recovery projects implemented in northern China, was the main cause of desertification reversion in this region. Therefore, ecological recovery projects are still required to promote harmonious development between nature and human society in ecologically fragile regions like the Ordos Plateau.

Keywords: semi-arid area; climate change; human activities; desertification; Ordos Plateau; remote sensing

1. Introduction

Desertification can be defined as land degradation in the arid, semi-arid and dry sub-humid areas resulting from climate change and human activities [1]. Desertification directly affects the wellbeing of over 250 million people and puts at risk the livelihoods of over one billion people around the world [2,3], making it one of the most serious environmental issues [1,4]. China is one of the most seriously affected countries with respect to desertification, especially in the northwestern part, where the desertification process has accelerated the loss of the agriculturally important fine fraction of the topsoil by wind erosion and has generated frequent dust storms [5,6]. The spread of desertification has caused economic losses and reduction of biodiversity, and it is detrimental to human health.

Quantitative measurement of diagnostic indicators of desertification and analysis of the driving factors are crucial for the control and rehabilitation of desertification [6–8].

The Ordos Plateau lies in the semi-arid farm-pastoral region of North-Central China. This area has long been affected by desertification under the influence of both poor climate conditions and human intervention. To improve the ecological environment of northern China, the Chinese government implemented the Grain for Green Program and the Return Grazing to Grass Program, among other ecological engineering projects that have proven beneficial to desertification reversion [9]. However, little is known about the quantitative relationship between the desertification trend and its driving factors, including climate change and human activities, which may hinder the development of rehabilitation strategies. Therefore, effective monitoring of the desertification status and a thorough understanding of the relative roles of the driving factors in the desertification process are fundamental for the control of desertification.

Field monitoring can provide useful information about the desertification process; however, its application is often limited due to its low spatial coverage. By comparison, remote sensing is a time- and cost-efficient way to extract explicit information at various temporal and spatial scales, and it has become a valuable tool for monitoring environmental change [10–12]. Multi-spectral satellite instruments such as Landsat have been acquiring imagery over the Earth since the 1970s, which makes them a potential tool for long-term continuous monitoring of desertification [12–15]. Temporal variations in vegetation directly represent the dynamics of biomass in arid and semi-arid ecosystems. Additionally, variations in vegetation are easy to interpret from satellite images. Thus, image-based vegetation indices are widely used as indicators in the assessment of desertification [16,17]. Particularly, the fraction of green vegetation cover, which can be calculated by the normalized difference vegetation index (NDVI), is now one of the two global indicators required for reporting by governments, according to the United Nations Convention to Combat Desertification (UNCCD) [18]. Landsat and similar satellite instruments can be used to measure and map NDVI, but their spectral bands are less suited for measuring both dry vegetation and bare soil components [19] which are more common surface components in dryland regions such as the Ordos Plateau. Thus, monitoring or assessing desertification using NDVI time series alone in dryland regions is problematic [20]. Researchers have also tried to use indices that are sensitive to the non-vegetation components exposed in soils and rocks, such as the bare soil index (BSI) [21] and the grain size index (GSI), in the assessment of desertification [22]. Other researchers have tried to incorporate these non-vegetated components into green vegetation indices, such as the soil-adjusted vegetation index (SAVI) and the modified SAVI (MSAVI) [16,17]. Land surface albedo is also a potential indicator for bare ground [23,24]. The combinations of these indices and/or the original reflectance data can be used as input for statistically modeling desertification status using various methods, including supervised classification [25], support vector machine [26] and decision tree [23,27] methods.

Although the dynamics of desertification status can be monitored and assessed using remote sensing images and assessment models, the driving forces in the desertification process are still being disputed [28,29]. Many studies have suggested that both climate change and human activities play important roles in the process of desertification [30,31]. However, distinguishing human-induced from climate-induced factors, or determining which of them is the primary cause during a certain period, is still a challenging task due to the complex mechanism of desertification. To achieve this goal, some studies have used vegetation indices such as NDVI and net primary productivity (NPP) to distinguish human-induced degradation or desertification from climate-induced change by comparing the potential and actual vegetation status [17,32,33]. Rain use efficiency (RUE), calculated as the ratio of NPP or NDVI to rainfall, has proven useful to relate the desertification process to its potential driving forces [16,34]. Residual trends (RESTREND) is another potential method, where a negative trend in residual values (the difference between observed and predicted NDVI based on rainfall) can be regarded as a sign of human-induced desertification [33,35]. Although these methods can identify the regions experiencing human-induced desertification, they cannot be used to quantitatively assess

the relative roles of climate change and human activities in desertification dynamics. Similar in essence to the RESTREND model, previous studies have shown that human appropriation NPP (HANPP) can be used to represent the effect of human activities on the ecosystem [36–39]. In their methods, the HANPP was defined as the difference between the climate-driven potential NPP (PNPP) and actual NPP (ANPP) simulated using both climate and remote sensing data. Based on this concept, desertification dynamics can be linked to their driving forces, with ANPP and HANPP denoting the impacts of climate change and human intervention, respectively [8,9,40]. This method provides a potential way to quantitatively assess the relative roles of climate change and human activities in the desertification dynamics.

The objectives of this study were: (1) to assess the desertification status from 2000 to 2015 based on indicators retrieved from Landsat data and a decision tree model; and (2) to quantitatively analyze the relative roles of climate change and human activities in the reversion and expansion process of desertification using NPP as the indicator.

2. Materials and Methods

2.1. Study Area

The Ordos Plateau (hereafter referred to as Ordos for short) is located in the southwest of the Inner Mongolia Autonomous Region (IMAR), China, ranging from 37°41′–40°51′N to 106°42′–111°31′E (Figure 1). It includes seven banners (county-level administrative divisions in the IMAR) and one urban district, covering an area of 86,882 km^2, with elevation varying from 1000 to 1500 m above sea level. Ordos has a typical semi-arid climate with a mean annual temperature of 5.3–8.7 °C and an annual sunshine duration of 2716–3194 h. The annual average precipitation ranges from 450 mm in the southeast to 150 mm in the northwest [41]. Moreover, most of the rainfall occurs from July to September.

The major parts of this area are the Kubuqi Desert on the northern margin of Ordos and the Mu Us sandy land, located in southeastern Ordos. The main land cover/use type is grassland, as shown in Figure 1, and the dominant plant species is *Artemisia ordosica*. The main soil types in this area include aeolian sandy soil, chestnut soil and brown soil.

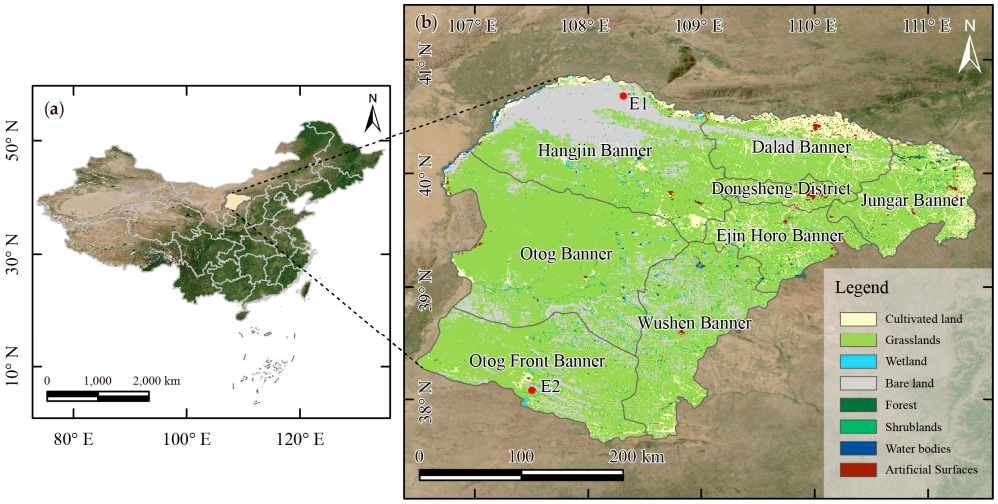

Figure 1. (**a**) Geographic location of the study area; (**b**) Land cover/use of the study area acquired from GlobeLand30 dataset (http://www.globallandcover.com/). Red dots marked E1 and E2 in sub-figure (**b**) show the locations of satellite images used in Figure 11 and Figure 13, respectively.

Ordos is a typical farming-pastoral area where agriculture and animal husbandry play important roles in the local economy. The population of Ordos grew from 1.31 million in 2000 to 1.57 million in 2015, according to the data released by the local bureau of statistics. This increase in population has

led to irrational use of land, such as extensive reclamation and over-grazing, which has exacerbated land degradation and the expansion of desertification.

2.2. Data Sources and Preprocessing

Landsat-5 Thematic Mapper (TM), Landsat-7 Enhanced Thematic Mapper Plus (ETM+) and Landsat-8 Operational Land Imager (OLI) images were used in this study. Landsat TM/ETM+ level-1 terrain-corrected (L1T) data of 2000, 2006, and 2010 and Landsat OLI L1T data of 2015 were used to assess the desertification of Ordos. Seven scenes (path/row: 127/32, 127/33, 128/32, 128/33, 128/34, 129/32 and 129/33) of Landsat data were employed to build a seamless mosaic imagery. These Landsat multi-spectral data were acquired from the United States Geological Survey (USGS) (http://glovis.usgs.gov/). To minimize the influences of vegetation phenology, these time series remote sensing data were obtained from August to September, when vegetation reaches its maximum during the growing season. Acquiring cloud-free images that cover the whole study area within a given year was difficult due to the large geographic coverage. Therefore, some images from previous or subsequent years were used to generate a cloud-free mosaic. The Landsat L1T product processing includes radiometric, geometric and precision corrections using ground control chips as well as the use of a digital elevation model to correct parallax error due to local topographic relief [42–44]. Therefore, we did not perform a geometric correction during the preprocessing. The original digital number (DN) values were firstly converted to the top of atmosphere (TOA) spectral radiance using the parameter information in the header file of Landsat TM/ETM+ [45] and Landsat OLI. The atmospheric correction was a critical pre-processing step in order to calculate the indicators for desertification assessment. In this study, atmospheric correction of the Landsat data was performed using the Fast Line-of-sight Atmospheric Analysis of Spectral Hypercubes (FLAASH) module embedded in the Environment for Visualizing Images (ENVI) software. The FLAASH module provides a unique solution for each image using the MODerate resolution atmospheric TRANsmission (MODTRAN4) radiative transfer code as the atmospheric radiation correction model with high precision. The mid-latitude summer atmospheric model was used to define the water vapor amount, and the rural aerosol model was selected to define the aerosol type. In addition, the "2-band (K-T)" option was selected for aerosol retrieval in the FLAASH module. After the atmospheric correction, the TOA radiance was converted to a surface reflectance value for each pixel.

NPP is a key indicator for assessing the relative roles of climate change and human activities in desertification dynamics. The monthly NDVI product (MOD13A3) derived from the Moderate Resolution Imaging Spectrometer (MODIS) multi-spectral data and ground-based meteorological data from 2000 to 2015 was used to estimate NPP. Meteorological data, including monthly average temperature, cumulative precipitation and the total solar radiation from 18 meteorological stations in and around Ordos were collected from the China Meteorological Administration (http://data.cma.cn/). Spline interpolation was employed to generate meteorological grid data to drive the NPP model.

2.3. Indicators for Desertification Assessment

Changes in the land surface, such as vegetation coverage and soil component, are closely related to desertification dynamics. Three multi-spectral indices calculated from Landsat images that are related to vegetation coverage or soil component were used as indicators for desertification assessment.

Several vegetation indices, such as the ratio vegetation index (RVI), normalized difference vegetation index (NDVI), soil-adjusted vegetation index (SAVI) and modified soil adjusted vegetation index (MSAVI) have been designed to quantitatively estimate the vegetation coverage or biomass. Among these indices, previous studies have shown that MSAVI is helpful because it can increase the dynamic range of the vegetation signal while minimizing the influence of background soil [46]. Thus, in order to quantify vegetation coverage, MSAVI was selected and calculated from the near-infrared (NIR) and red (R) bands of Landsat multi-spectral data as the following formula:

$$\mathrm{MSAVI} = (2\rho_{\mathrm{NIR}} + 1 - \sqrt{(2\rho_{\mathrm{NIR}} + 1)^2 - 8(\rho_{\mathrm{NIR}} - \rho_{\mathrm{R}})})/2 \quad (1)$$

where ρ_{NIR} and ρ_{R} stand for spectral reflectance measurements acquired in the near-infrared and visible red bands, respectively.

BSI can be used for mapping bare soil and distinguishing it from vegetation cover. Generally, BSI increases with increasing bare soil exposure of the land surface during the expansion of desertification. Moreover, as a normalized index that can combine both bare soil and vegetation indices, BSI can be used to assess the status of vegetation coverage, ranging from high vegetation to exposed soil condition [21,47]. This alleviates the problem where the value of the vegetation index can be unreliable when there is sparse vegetation. Thus, BSI can be used to investigate land degradation and desertification processes. Here, BSI was calculated using the following equation [47]:

$$\mathrm{BSI} = \frac{(\rho_{\mathrm{SWIR}} + \rho_{\mathrm{R}}) - (\rho_{\mathrm{NIR}} + \rho_{\mathrm{B}})}{(\rho_{\mathrm{SWIR}} + \rho_{\mathrm{R}}) + (\rho_{\mathrm{NIR}} + \rho_{\mathrm{B}})} \times 100 + 100 \quad (2)$$

where ρ_{B}, ρ_{R}, ρ_{NIR}, and ρ_{SWIR} stand for the spectral reflectance values of Band 1, Band 3, Band 4, and Band 5 for the Landsat TM/ETM+ data and Band 2, Band 4, Band 5, Band 6 for the Landsat OLI data, respectively.

Land surface albedo can be defined as the instantaneous ratio of surface-reflected radiation flux to the incident radiation flux over the shortwave spectral domain [48]. It is an important indicator to determine the change of surface conditions such as temperature and aridity/humidity in desertification dynamics. In general, replacing vegetation with bare soil causes an increase in land surface albedo, and this increase in albedo implies degradation or desertification [22,49,50]. Therefore, albedo is also employed to assess the dynamics of desertification. The albedo can be calculated using a linear combination of the monochromatic reflectance values through the reflective bands [48]:

$$\mathrm{Albedo} = 0.356\rho_{\mathrm{B}} + 0.130\rho_{\mathrm{R}} + 0.373\rho_{\mathrm{NIR}} + 0.085\rho_{\mathrm{SWIR1}} + 0.072\rho_{\mathrm{SWIR2}} - 0.0018 \quad (3)$$

where ρ_{B}, ρ_{R}, ρ_{NIR}, ρ_{SWIR1}, and ρ_{SWIR2} stand for spectral reflectance values of Band 1, Band 3, Band 4, Band 5 and Band 7 for the Landsat TM/ETM+ and Band 2, Band 4, Band 5, Band 6 and Band 7 for the Landsat OLI, respectively.

2.4. Desertification Dynamics Assessment

The desertification of the land surface can be divided into five grades: non-desertification, slight, moderate, high and severe desertification, according to a frequently used grading system in China [51]. In this study, the C5.0 decision tree (DT) model was employed to construct a classification model and to identify the grades of desertification by using the combination of indicators calculated using Landsat data. This model can classify large amounts of data according to the established division rules, and it allows for visualizing the tree structure rule sets, making it widely applicable [52].

A training set of records tagged with decision labels and containing a group of attribute values is firstly required to build a decision tree. In this study, over one hundred training points for each desertification grade were selected as an input sample data set according to the Atlas of Desertified and Sandified Land in China and visual interpretation of satellite images. By using this input sample data set, the information gain ratio criterion of the C5.0 model was engaged to determine the optimal thresholds of each indicator for separating different desertification grades [53,54]. A set of tree-like rules was produced using this method. The results obtained by the training procedure, however, may perform poorly due to errors in the dataset. To reduce the errors during processing, a newly built decision tree has to be pruned back. In the C5.0 model, pruning starts automatically on leaf nodes and spreads upward to the whole tree using the information gain ratio. Further details on the pruning methods can be found elsewhere [54,55]. Finally, the pruned hierarchically structured rules (Figure 2) were applied to assess the status of desertification.

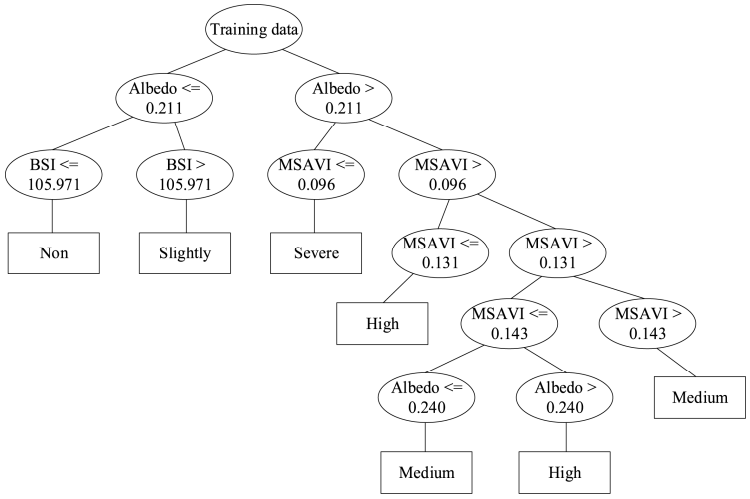

Figure 2. Statistically developed decision tree for the assessment of desertification status. MSAVI: modified soil adjusted vegetation index; BSI: bare soil index.

2.5. Calculation of Actual and Potential NPP

The actual NPP (ANPP) was calculated using the Carnegie-Ames-Stanford Approach (CASA) model, a light-use efficiency model based on the resource-balance theory [56,57]. This model has been proven feasible and accurate in simulating the NPP compared with observed values and has been widely used in China [58]. Monthly NPP was obtained by the CASA model and then the annual NPP (gC m^{-2} yr^{-1}) was calculated by the sum of monthly NPP within a year. In the CASA model, NPP is calculated using the following equation:

$$\mathrm{NPP}(x,\ t) = \mathrm{APAR}(x,\ t) \times \varepsilon(x,\ t) \tag{4}$$

where NPP(x, t) represents the NPP in the geographic coordinate of a given location x and time t, APAR(x, t) (MJ m^{-2}) represents the canopy absorbed incident solar radiation integrated over a given period, and ε (gC MJ^{-1}) is the actual light-use efficiency (LUE). APAR can be calculated using the following equation:

$$\mathrm{APAR}(x,\ t) = \mathrm{SOL}(x,\ t) \times \mathrm{FPAR}(x,\ t) \times 0.5 \tag{5}$$

where SOL(x, t) is the total solar radiation and FPAR(x, t) is the fraction of photosynthetically active radiation absorbed by vegetation, which can be determined by NDVI. The constant 0.5 represents the proportion of the total solar radiation available for vegetation. The LUE can be expressed as follows:

$$\varepsilon(x,\ t) = T_{\varepsilon 1}(x,\ t) \times T_{\varepsilon 2}(x,\ t) \times W_{\varepsilon}(x,\ t) \times \varepsilon_{\max} \tag{6}$$

where $T_{\varepsilon 1}(x, t)$ and $T_{\varepsilon 2}(x, t)$ denote the temperature stress coefficients, which reflect the reduction of LUE caused by the temperature factor, $W_{\varepsilon}(x, t)$ is the moisture stress coefficient, which indicates the reduction of LUE caused by the moisture factor, and ε_{max} is the maximum LUE value under ideal conditions set as different values for various land types [59]. A more detailed description of this algorithm can be found in [60].

To validate the estimation accuracy of the CASA model, we compared the simulated NPP values of 2006 to the MODIS annual NPP product (MOD17A3) in the study area. We selected the MODIS NPP product as the reference because it has been validated as consistent with field-observed values, and the product can capture the NPP pattern across various biomes and climate regimes [61]. Figure 3 illustrates the comparison of the two datasets. The results show a high degree of consistency for the two datasets, with the R^2 exceeding 0.8 at a high significance level of $p < 0.001$. Yet, the CASA modeled data were slightly higher than the MODIS estimates, which can be partially explained by the fact

that the MOD17 product tends to underestimate NPP in China [62,63]. Nevertheless, we deemed it appropriate to utilize the CASA-simulated NPP in the time-series trend analysis.

In this study, the potential NPP (PNPP with no human disturbance) was simulated using the Thornthwaite memorial model [64], which is expressed as follows:

$$\mathrm{NPP} = 3000(1 - e^{-0.0009695(v-20)}) \tag{7}$$

$$v = \frac{1.05r}{\sqrt{1 + (1 + 1.05r/L)^2}} \tag{8}$$

$$L = 3000 + 25t + 0.05t^3 \tag{9}$$

where NPP is the potential annual NPP (gC m^{-2} yr^{-1}), r denotes the annual total precipitation (mm), and t is the annual average temperature (°C).

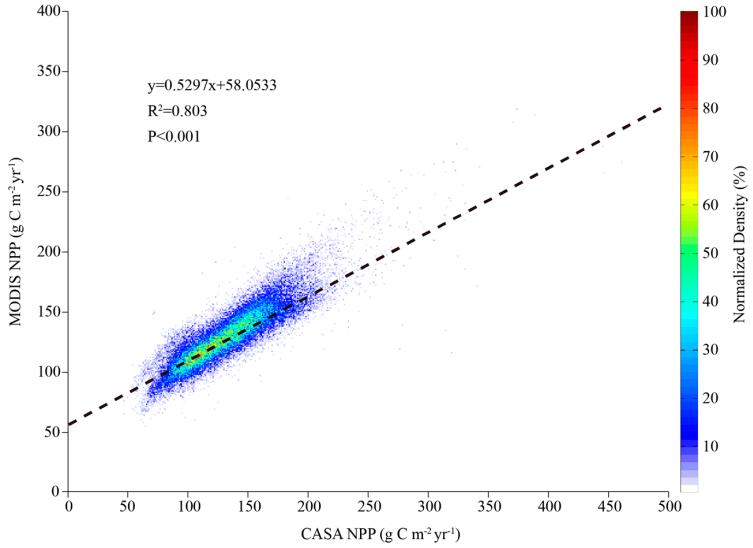

Figure 3. Comparison of Carnegie-Ames-Stanford Approach (CASA)-simulated net primary productivity (NPP) with the Moderate Resolution Imaging Spectrometer (MODIS) annual NPP product (MOD17A3) in the year 2006.

2.6. Quantitative Assessment of the Relative Roles of Climate Change and Human Activities in Desertification Dynamics

As an important ecological indicator for estimating vegetation production, NPP reflects the complex interactions between climate change and human activities. We used yearly total NPP to assess the relative roles of climate change and human activities in the desertification dynamics. The effect of climate change on NPP was measured based on the temporal trend of PNPP. The effect of human activities on NPP was measured using the trend of human appropriation NPP (HANPP, i.e., PNPP-ANPP, denoting the NPP loss caused by human intervention). For analysis of the trends, the slopes (referred to as S_P and S_H, respectively) of a period from year t to year $t + n$ were calculated by ordinary least squares regression using the following equation:

$$\mathrm{Slope} = \frac{n\sum xy - \sum x \sum y}{n\sum x^2 - (\sum x)^2} \tag{10}$$

where x is year, y is PNPP or HANPP, and n is the time span. For the areas identified as experiencing desertification reversion or expansion, the relative roles of climate change and human activities can be mapped on a grid scale by analyzing the S_P and S_H using the possible scenarios defined in Table 1.

A positive S_P or negative S_H trend indicates that the effect of climate change or human activities during the period of year t to $t + n$ is beneficial to vegetation growth and desertification reversion. Conversely, a negative S_P or positive S_H trend indicates that the effect of climate change or human activities is beneficial to vegetation degradation and desertification expansion. In the situation of desertification reversion, if S_P and S_H are both positive (Scenario 1), the reversion can be attributed to climate change entirely. If S_P and S_H are both negative (Scenario 2), the reversion can be attributed to human activities entirely. If S_P is positive and S_H is negative (Scenario 3), the reversion is considered the combined result of climate change and human activities. In this situation, the individual contributions of the two factors can be calculated using the relative ratio of S_P and S_H. The scenarios for desertification expansion are also shown in Table 1.

Table 1. Scenarios for assessing the roles of climate change and human activities in desertification. S_P: slope of potential NPP (PNPP); S_H: slope of human appropriation NPP (HANPP).

		S_P	S_H	Relative Role of Climate Change (%)	Relative Role of Human Activities (%)
Desertification reversion	Scenario 1	+	+	100	0
	Scenario 2	−	−	0	100
	Scenario 3	+	−	$\frac{\lvert S_P \rvert}{\lvert S_P \rvert + \lvert S_H \rvert} \times 100\%$	$\frac{\lvert S_H \rvert}{\lvert S_P \rvert + \lvert S_H \rvert} \times 100\%$
	Scenario 4	−	+	Error	Error
Desertification expansion	Scenario 1	−	−	100	0
	Scenario 2	+	+	0	100
	Scenario 3	−	+	$\frac{\lvert S_P \rvert}{\lvert S_P \rvert + \lvert S_H \rvert} \times 100\%$	$\frac{\lvert S_H \rvert}{\lvert S_P \rvert + \lvert S_H \rvert} \times 100\%$
	Scenario 4	+	−	Error	Error

3. Results

3.1. Dynamics of Desertification in Ordos between 2000 and 2015

The assessment results of desertification grades for the four periods are shown in Figure 4, and the resultant statistical data are shown in Table 2 (the numbers 1, 2, . . . , 7 in Figure 4 represent Hangjin, Otog, Otog Front, Dalad, Ejin Horo, Wushen and Jungar Banner, respectively, and the number 8 represents the Dongsheng District). From 2000 to 2006, the slight desertification area roughly doubled from 13,943 km^2 to 30,389 km^2. The non-desertification area fell by 9.3% from 6647 km^2 to 6027 km^2. Meanwhile, the moderate, high and severe desertification areas decreased by 36.5%, 13.7% and 27%, respectively. This significant decrease indicates that the study area experienced a recovery trend overall despite the fact that the total desertification area increased from 80,256 km^2 to 80,876 km^2. The areas of moderate, high and severe desertification showed a diminishing trend, with their areas decreasing by 44.1%, 20.5% and 28.8%, respectively, during 2006 to 2010. Conversely, the areas of non- and slight desertification increased by 72.6% and 32.8% during the same period, which suggests a steady trend of recovery. During 2010–2015, the areas of non-, moderate and high desertification experienced an increasing trend, while the others decreased on different levels, as shown in Table 2. During 2000 to 2015, the area of non-desertification increased from 6647 km^2 to 15,961 km^2, with an annual growth rate of 6%. Meanwhile, the area of severe desertification fell at an annual rate of 4.3%, from 16,161 km^2 to 8331 km^2. The gradual increase of non-desertification area and decrease of severe desertification area suggests that the desertification status of Ordos has reversed in the past 15 years.

Table 2. The status of desertification in Ordos during various periods (area: km^2; proportion: %).

	2000		2006		2010		2015	
	Area	Proportion	Area	Proportion	Area	Proportion	Area	Proportion
Non	6647	7.65	6,027	6.94	10,424	11.99	15,961	18.37
Slight	13,943	16.04	30,389	34.97	40,350	46.43	32,700	37.63
Moderate	20,176	23.22	12,814	14.75	7163	8.24	8553	9.84
High	29,976	34.49	25,878	29.78	20,566	23.67	21,358	24.58
Severe	16,161	18.6	11,795	13.56	8400	9.67	8331	9.58

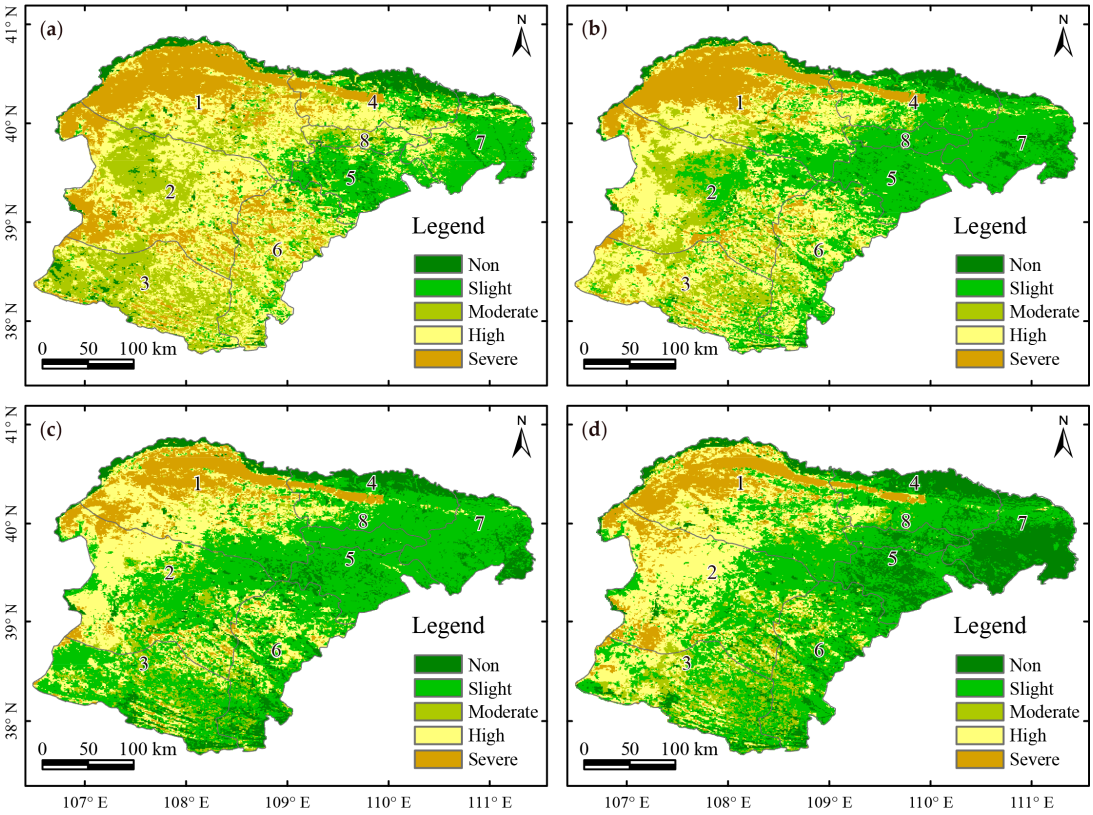

Figure 4. Desertification assessment results of four periods: (**a**) 2000; (**b**) 2006; (**c**) 2010 and (**d**) 2015.

By further processing the assessment results using "Change Detection" incorporated in ENVI, the desertification change maps for 2000–2006, 2006–2010 and 2010–2015 were obtained, as shown in Figure 5. For better interpretation of the dynamics, we classified the dynamic changes into five categories: an increase or decrease in the desertification grade relative to its neighboring grade (e.g., a change from slight to moderate) indicates "developed" or "reversed"; a cross-level increase or decrease (e.g., a change from slight to high desertification) indicates "seriously developed" or "significantly reversed"; and no change in grades during two periods indicates "stable".

During 2000 to 2006, the regions of developed and seriously developed desertification were mainly distributed in the west boundary of Hangjin and Otog Banner as well as the west part of Otog Front Banner. These regions had a land area of 4985 km^2 in total. During the same period, 17,014 km^2 of desertification land was reversed or significantly reversed and was basically distributed in eastern Otog Banner and the common boundary of Dalad, Jungar Banner and Dongsheng District. From 2006 to 2010, 3178 km^2 of desertification land was developed, seriously developed or converted to desertification land from non-desertification land and was mainly distributed in the northern Otog Banner and southern Hangjin Banner. Meanwhile, a total of 15,048 km^2 of desertification land was reversed or significantly reversed and was mainly distributed in Otog Front and Wushen Banner. The total area of reversed and significantly reversed land was 4.7 times that of developed and seriously developed land, suggesting the significant recovery trend during this period. From 2010 to 2015, approximately 7562 km^2 of desertification land developed, seriously developed or converted to desertification land from non-desertification land, and this area was distributed in the central Otog Banner and western Otog Front Banner. During the same period, approximately 10,180 km^2 desertification land was reversed or significantly reversed and was primarily distributed in Jungar Banner, central Hangjin and Ejin Horo Banner.

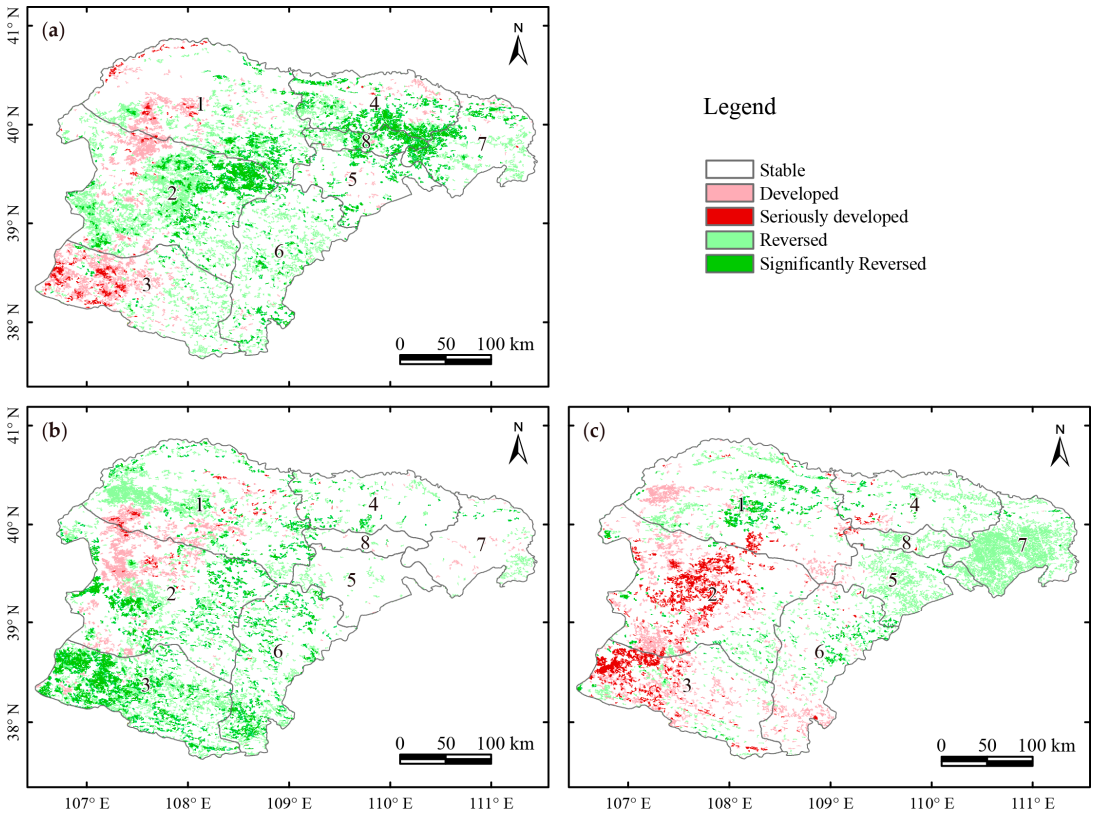

Figure 5. Spatial distribution of desertification dynamics for (**a**) 2000–2006; (**b**) 2006–2010 and (**c**) 2010–2015.

3.2. *Relative Roles of Climate Change and Human Activities in Desertification Reversion*

Based on the identified areas that experienced desertification reversion, the relative roles of climate change and human activities in various periods were mapped by analyzing the temporal trends of PNPP and NANPP according the scenarios defined in Table 1. The relative roles of these two factors showed obvious temporal and spatial heterogeneity. During the period 2000–2006, the areas that experienced reversion mainly caused by climate change (the relative role of climate change greater than 50%) account for 43.0% of the whole reversed area. These areas were mainly distributed in Dalad, Jungar, western Hangjin and western Otog Banner, as shown in Figure 6. Meanwhile, the areas that experienced reversion mainly caused by human activities (the relative role of human activities greater than 50%) account for 56.3% of the whole reversed area as shown in Figure 7, and they were mainly distributed in Otog Front, Wushen, and eastern Otog Banner. Proportionately, the relative roles of climate change and human activities in desertification reversion were not much different for the study area as a whole. From 2006 to 2010, however, in most areas, including Hangjin, Dalad, Jungar, Otog and Otog Front Banner, the reversion was mainly induced by human activities. These areas amounted to 87.3% of the whole region that experienced desertification reversion in Ordos. In the same period, only 11.4% of the total reversed land was mostly caused by climate change. From 2010 to 2015, human activities were also the major cause of reversion in central Hangjin, Dalad, Jungar, Ejin Horo, Wushen Banner and Dongsheng District. Few regions that had experienced desertification reversion mainly caused by climate change were distributed in northern Hangjin, western Otog and western Otog Front Banner. The reversed regions dominated by human activities and climate change amounted to 91.7% and 8.0% of the whole reversed land, respectively.

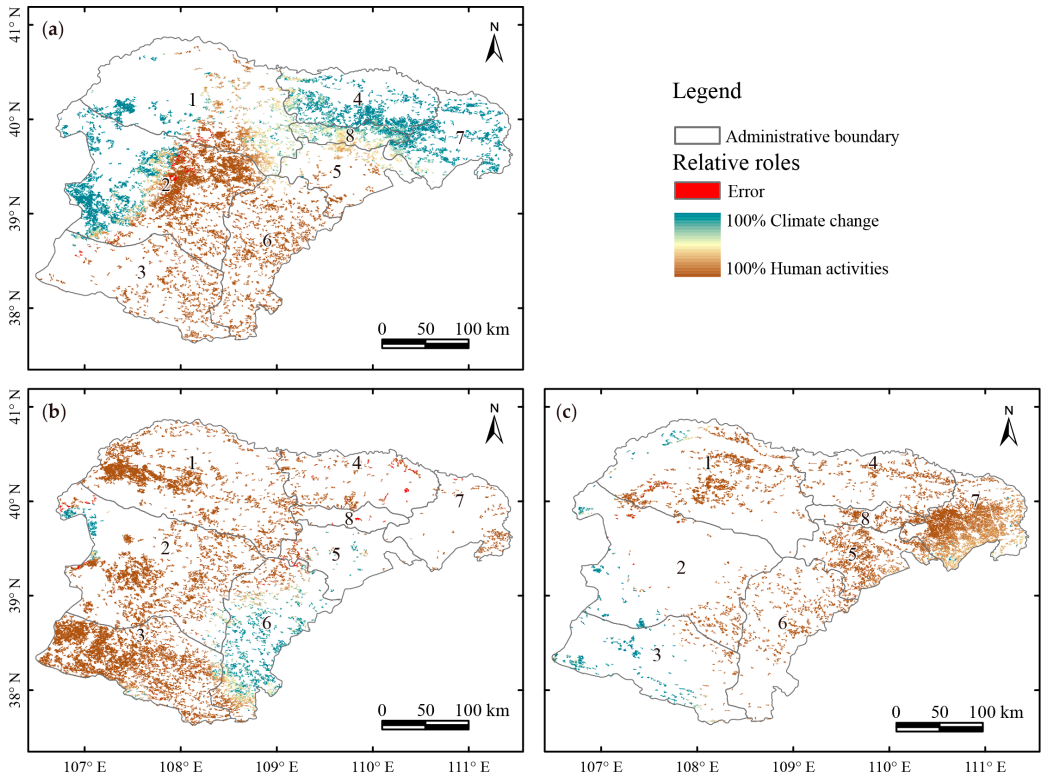

Figure 6. The relative roles of climate change and human activities in desertification reversion for (**a**) 2000–2006; (**b**) 2006–2010 and (**c**) 2010–2015.

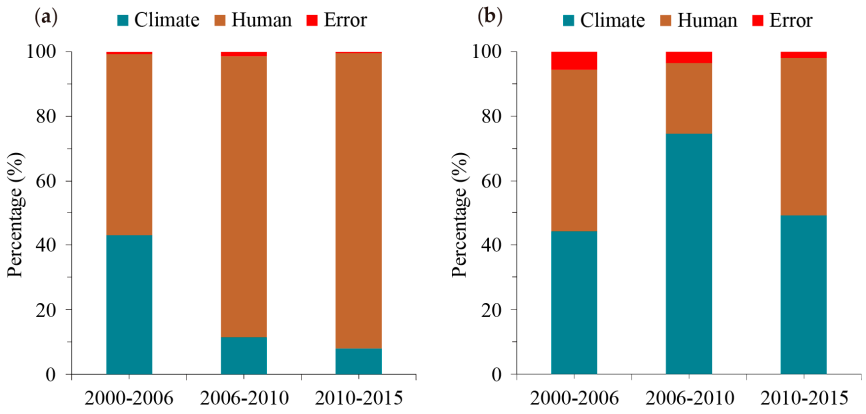

Figure 7. Contributions of climate change and human activities in various periods for (**a**) desertification reversion and (**b**) expansion.

3.3. Relative Roles of Climate Change and Human Activities in Desertification Expansion

Similar to desertification reversion, the process of desertification expansion in various periods was spatially linked to its driving forces on a grid scale, as shown in Figure 8. Human activities and climate change both played large roles in the desertification expansion from 2000 to 2006. The regions that experienced desertification expansion dominated by human activities were mainly distributed in the common boundary of Hangjin and Otog Banner and accounted for 50.3% of the total degraded area. Meanwhile, the regions that experienced desertification expansion dominated by climate change were mainly distributed in western and central Otog Front Banner and accounted for 44.2% of the total degraded area. Nevertheless, from 2006 to 2010, climate change was the dominant factor controlling the desertification expansion process. In total, 74.6% of the degraded land was mainly

caused by climate change, and these areas were mainly distributed in Hangjin and western Otog Banner. Only 21.9% of the degraded land was controlled by human activities, and it was mainly concentrated in northwestern Otog Banner. During the period 2010 to 2015, climate change was the principal cause of desertification expansion in southern Hangjin, central Otog and Wushen Banner, whereas human activities dominated the expansion in western Hangjin, southwestern Otog, and western Otog Front Banner. The desertification expansion mainly induced by climate change and human activities during this period accounted for 49.1% and 49.0% of the total degraded land, respectively.

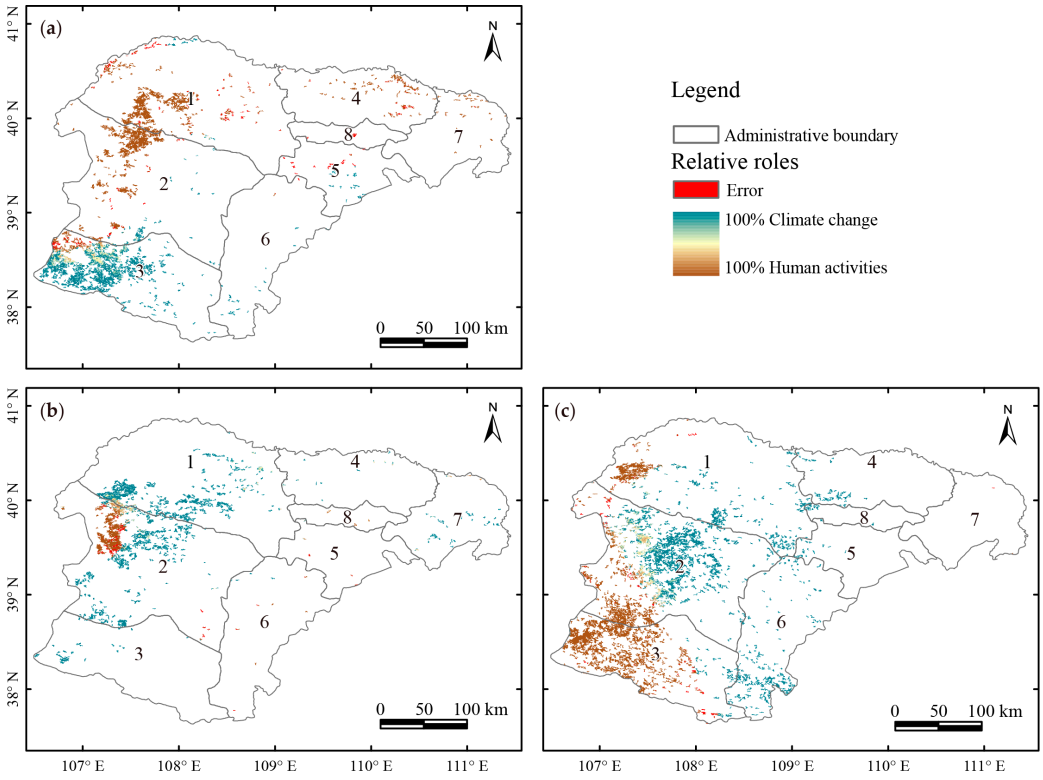

Figure 8. The relative roles of climate change and human activities in desertification expansion for (**a**) 2000–2006, (**b**) 2006–2010 and (**c**) 2010–2015.

4. Discussion

Based on the three retrieved indicators (MSAVI, BSI and albedo), a decision tree model was built to assess the status of desertification in Ordos by referencing the published atlas of desertification monitoring along with visual interpretation. An accuracy check of the model was carried out using a group of random selected validation samples. The result showed satisfactory accuracy (91%), suggesting the suitability of the decision tree model in this study. Our assessment results revealed that even though some regions experienced desertification expansion, the desertification status in Ordos showed a recovery trend from 2000 to 2015, which is consistent with some studies conducted in arid and semi-arid areas of China [9].

Analyzing the driving mechanism of desertification carries theoretical and practical significance for the prevention and alleviation of desertification. The dynamics of desertification result from the comprehensive effects of climate change and human intervention. Distinguishing the human impacts on desertification dynamics from those of climate change is still a problem that needs to be solved [17]. In this study, the dynamics of desertification were linked to these two kinds of driving forces by comparing the temporal trend of PNPP and HANPP. Based on the scenarios that describe all the combinations of desertification status changes and the trends of PNPP and HANPP as shown in Table 2, the relative roles of climate change and human activities were quantitatively assessed.

As shown in Figures 6 and 8, the quantitative assessment result incorporated some "error" regions defined in Table 1. The "error" was defined as regions that experienced desertification expansion when both climate change and human activities were conducive to the reversion, and regions that experienced desertification reversion when both climate change and human activities were conducive to the expansion. These assessment errors were inevitable, because completely accurate classification or monitoring of the desertification status could not be achieved. Moreover, the uncertainty of the climate data and the interpolation method, along with the uncertainty of NPP modeling, may have led to errors in the assessment. The proportions of "error" regions to the total reversed desertification land over the three periods 2000–2006, 2006–2010 and 2010–2015 were 0.7%, 1.3% and 0.3%, respectively, as shown in Figure 7. During the same periods, the proportions of "error" regions to the total expanded desertification land were 5.5%, 3.5% and 1.9%, respectively. These "error" regions would not have affected the overall results for the study area, due to their tiny proportions.

The effects of climate change, including the variations in annual precipitation and temperature, have a great influence on vegetation growth and further affect the expansion and reversion of desertification. Recently, studies have shown that since the 1980s, the temperature in northwestern China has undergone an increasing trend [65]. In line with the warming trend, the precipitation has also experienced an increasing trend in northwestern China [66]. In the current study, the annual temperature and precipitation of the entire study area was calculated by averaging the records from all 18 meteorological stations in and around Ordos. As shown in Figure 9, the average temperature and the overall average annual precipitation had an upward trend over the period 2000–2015, which is consistent with the previous reports. The warm, humid climate trend is beneficial to desertification reversion in the long run. However, this longtime trend cannot adequately explain the dynamics of desertification in the study area, due to the spatial and temporal heterogeneity of the climate factors. For instance, our results showed that, proportionally, human activity rather than climate change played the main role in desertification reversion during the period 2000 to 2015 for the study area as a whole. In fact, the effects of climate change in different regions and periods varied greatly, and these differences caused variations in the trend of PNPP, which was used to reflect the effect of climate change in desertification dynamics.

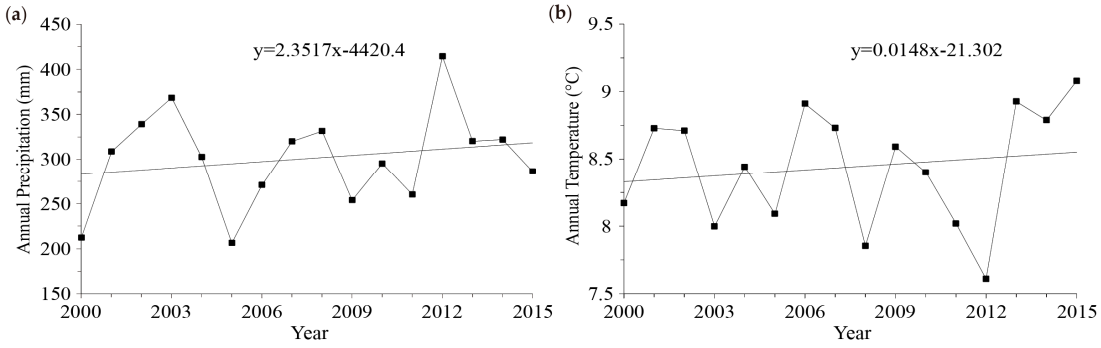

Figure 9. The trends of (**a**) annual precipitation and (**b**) temperature in the study area from 2000 to 2015 using the averaged data acquired from meteorological stations.

Driven by population growth and economic development, the sprawl of built-up areas causes the decline of natural vegetation cover [67]. In mineral-rich regions like Ordos, mining operations could also lead to vegetation degradation [68,69]. Moreover, human activities such as over-grazing, over-reclamation and excessive cutting of woody plants induce the loss of ecosystem equilibrium and the expansion of desertification. Meanwhile, human activities such as reforestation of cultivated land and banning of grazing can be beneficial to the reversion of desertification. To mitigate land degradation and desertification, the Chinese government has implemented many ecosystem programs, including the Grain for Green Program, in operation since 1999, the Beijing and Tianjin Sand Source

Control Project since 2002 and the Return Grazing to Grass Program since 2003. Under these ecosystem programs, the local government took some long-term measures, such as artificial afforestation and aerial sowing, to restore the ecological environment. Compared to artificial afforestation, aerial sowing is a mechanized afforestation approach that uses planes to spread tree or grass seeds. Closing land for afforestation is another strategy for the restoration of vegetation cover. In areas where natural sowing occurs, the lands are closed with the use of fences or barriers to exclude most forms of human exploitation for some years. Under favorable conditions, the ecological environment in the closed areas will improve during the closure period. According to the statistical yearbooks of Ordos, the area of annual artificial afforestation and aerial sowing (AAAS) in Ordos reached 209 km^2 in 2001 and remained approximately 50 km^2 per year in recent years, as shown in Figure 10. Moreover, the cumulative area of closed land for reforestation (CLR) surged from 55 km^2 in 2004 to 295 km^2 in 2014. The continuous implementation of ecological programs supports our finding that human activities were the dominant factor that led to desertification reversion during 2000 to 2015. Other studies have also shown the great impact of human factors on desertification reversion [8,9].

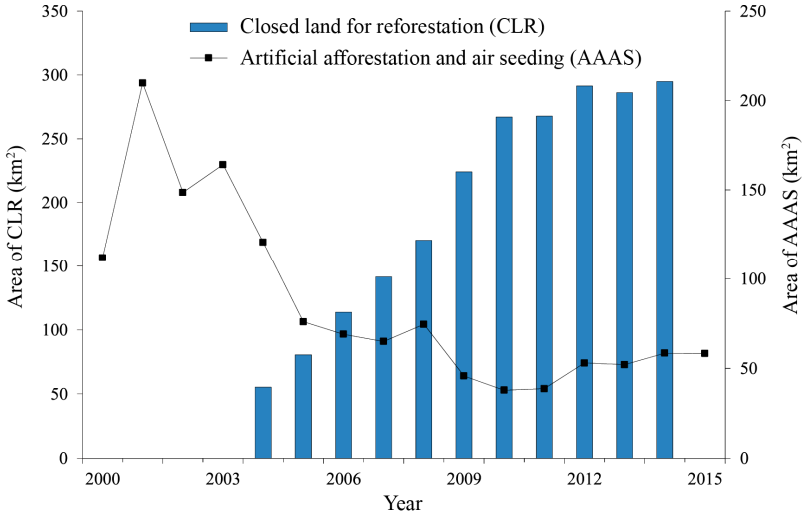

Figure 10. The area of closed land for reforestation (CLR) and the area of annual artificial afforestation and air seeding (AAAS) in Ordos.

Similar to the RESTREND model, in essence, the regions that experienced human-induced desertification expansion and reversion were identified by analyzing the trends of HANPP. However, the validation of the results was difficult, and field investigation and high resolution remote sensing data were needed [9,17]. In this study, one example site (the red dot marked E1 in Figure 1) that underwent human-induced desertification reversion and another site (the red dot marked E2 in Figure 1) that underwent human-induced desertification expansion were used to validate our results.

Figure 11 shows the human-induced desertification reversion around Qixing Lake, located in the north of the Kubuqi Desert, identified by our method and interpreted by comparing an Advanced Spaceborne Thermal Emission and Reflection Radiometer (ASTER) image acquired in 2010 and the Chinese Gaofen-2 (GF-2 a high-resolution optical earth observation satellite launched in August 2014) image acquired in 2015. To learn more about the status of desertification in the study area, a field campaign was conducted in July 2016. We found that the reversion in this area was due to the planting of local cold-arid-alkaline-resistant vegetation conducted by the Elion Group, a leading Chinese company specialized in land remediation and ecological rehabilitation. Bordered by the Yellow River to the west, north and east, the Kubuqi is rich in groundwater: despite the surface desolation, the ground is comparatively moist just a few feet below the surface. Thus, the indigenous vegetation, such as poplars and sand willows, can survive and thrive. As shown in Figure 12, willows

and grass were planted using underground water pumped from wells for irrigation. The afforestation led to vegetation reversion, and this was detected by our model, as shown in Figure 11. By means of its ecosystem restoration model, Elion has turned more than 11,000 km^2 of degraded land into productive land. The group tried to create a path of sustainable development in the Kubuqi desert that combines ecology, livelihood and economy. However, the sustainability of the restoration model in Kubuqi is still questionable, taking into account the fact that the underground water level has fallen steady in recent decades, according to interviews with local people. Further studies are still needed to achieve an equilibrium between afforestation and the available water supply and to ensure an ecologically sustainable relationship between nature and human society.

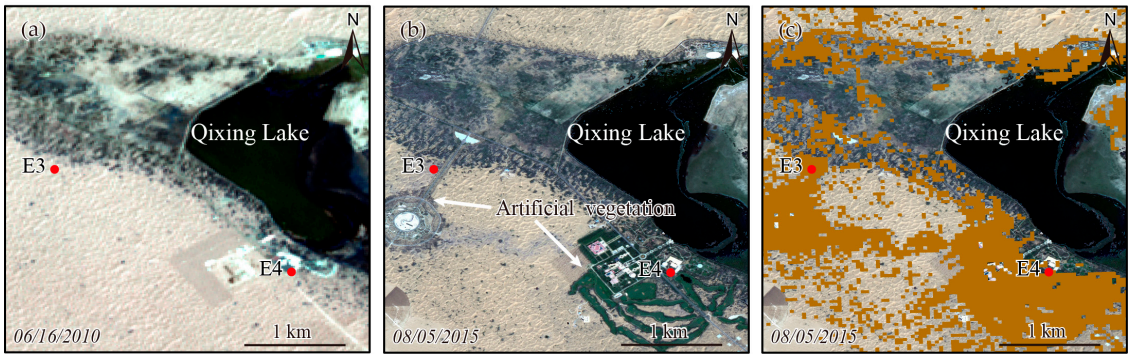

Figure 11. Human-induced desertification reversion and its validation. (**a**) Advanced Spaceborne Thermal Emission and Reflection Radiometer (ASTER) image acquired in 2010; (**b**) Gaofen-2 (GF-2) image acquired in 2015; (**c**) the areas identified in this study as experiencing human-induced desertification reversion (brown color) during 2010 to 2015. The red dots marked E3 and E4 show the locations of the photos used in Figure 12a,b.

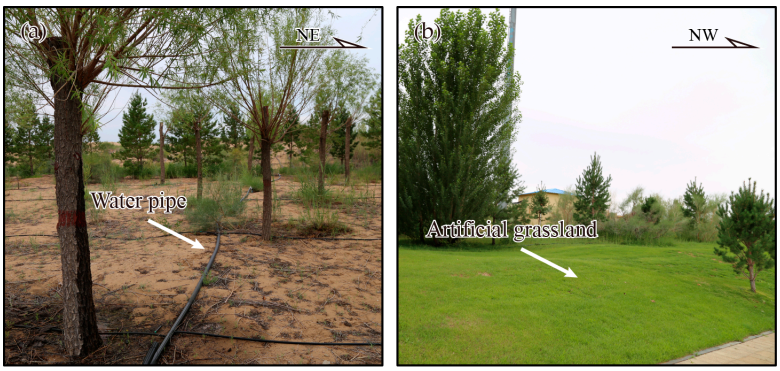

Figure 12. Photos showing the desertification reversion induced by afforestation (**a**) and grass planting (**b**). Their locations are shown in Figure 11.

Figure 13 shows the desertification expansion during 2006 to 2015 caused by increasing human activities detected in this study and the validation by comparing the Google Earth image acquired in 2003 and the GF-2 image acquired in 2015. We hypothesized that the vegetation did not change much from 2003 to 2006, and we used the image of 2003 to represent the desertification status of 2006. As shown in Figure 13, the dynamics of vegetation on the two sides of the fence line varied greatly. Outside of the fence line, the natural vegetation shows a recovery trend without human intervention. Inside the fence line, however, the vegetation shows a degradation trend as the result of over-grazing by livestock such as goats and sheep. This can be clearly seen in Figure 14. Apparently, our results well identified the effects of human activities in desertification expansion.

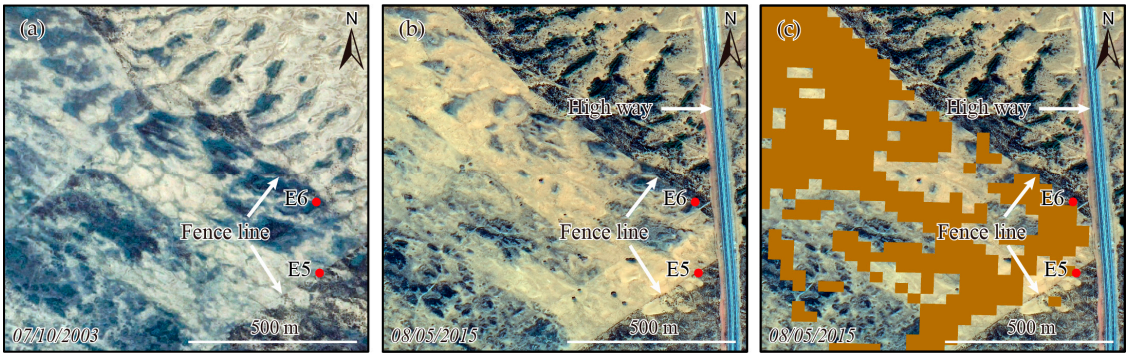

Figure 13. Satellite images showing the desertification expansion caused by stock breeding in Otog Front Banner, Ordos. (**a**) Google Earth image acquired in 2003; (**b**) GF-2 image acquired in 2015; (**c**) the area of human-induced desertification (brown color) during 2006 to 2015. The red dots marked E5 and E6 show the locations of the photos used in Figure 14a,b.

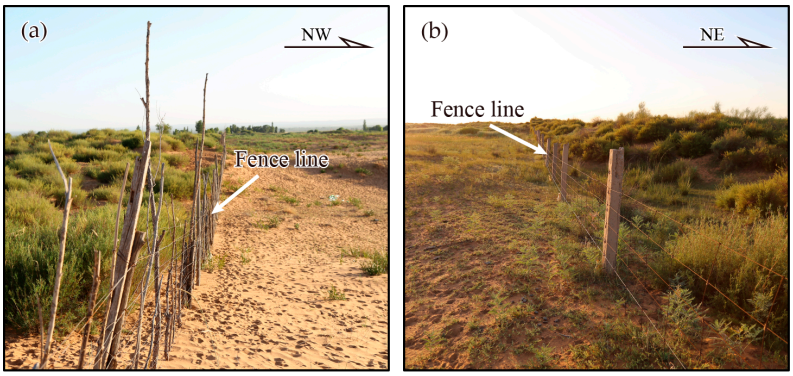

Figure 14. Photos showing the desertification expansion caused by stock breeding on the northwest (**a**) and southwest (**b**) of the fence line. Their locations are shown in Figure 13.

5. Conclusions

In this study, a satellite-based method integrated with the decision tree model was employed to monitor the dynamics of desertification degree and coverage. Furthermore, PNPP and HANPP estimated from the CASA model were used to measure the effects of climate change and human activities in the desertification process. This method can effectively identify areas that have undergone desertification reversion and expansion, and it can quantitatively assess the relative roles of the driving factors at a regional scale.

Our results based on Landsat images presented a recovery trend over the period 2000–2015 in Ordos, with the area of desertification land decreasing from 80,256 km^2 to 70,942 km^2. Temporally, human activities, especially the implementation of ecological restoration programs, mainly caused the desertification reversion from 2000 to 2015 for the study area as a whole. Climate change (including variations in precipitation and temperature) was the main factor causing the desertification expansion during 2006 to 2010. However, over the periods 2000–2006 and 2010–2015, the effects of climate change and human activities played roughly equal roles in the desertification expansion. Spatially, climate change and human activities were both responsible for the dynamics of desertification, but their relationships with desertification reversion and expansion showed a significant spatial heterogeneity. Therefore, different scenarios are required according to the local situations in order to mitigate desertification and realize the sustainable development.

This study indicates that climate change is a key factor influencing the dynamics of desertification, and human activities can help mitigate the desertification locally in arid and semi-arid regions such as the Ordos Plateau. For example, the afforestation implemented around Qixing Lake in the north

Kubuqi Desert can improve the local ecological environment. On the other hand, human activities such as stock breeding can aggravate the land degradation process, which policy-makers must keep in mind when making regional ecological conservation decisions and plans. The method used in this study could shed light on the mechanism of desertification and could be used to further develop efficient measures to combat desertification in the arid and semi-arid regions.

Acknowledgments: This work was supported by the CAS-CSIRO Cooperative Research Program (Grant No. GJHZ1407).

Author Contributions: Bihong Fu and Qiang Guo designed the analyses and contributed to the remote sensing data processing. Qiang Guo and Bihong Fu wrote the paper with contributions from all co-authors.

Conflicts of Interest: The authors declare no conflicts of interest.

References

1. United Nations Convention to Combat Desertification (UNCCD). *United Nations Convention to Combat Desertification in Countries Experiencing Serious Drought and/or Desertification, Particularly in Africa*; United Nations: Paris, France, 1994.
2. Adger, W.N.; Benjaminsen, T.A.; Brown, K.; Svarstad, H. Advancing a political ecology of global environmental discourses. *Dev. Chang.* **2001**, *32*, 687–715. [CrossRef]
3. Reynolds, J.F.; Stafford Smith, D.M.; Lambin, E.F.; Turner, B.L.; Mortimore, M.; Batterbury, S.P.J.; Downing, T.E.; Dowlatabadi, H.; Fernandez, R.J.; Herrick, J.E.; et al. Global desertification: Building a science for dryland development. *Science* **2007**, *316*, 847–851. [CrossRef] [PubMed]
4. Thomas, D.S.G. Science and the desertification debate. *J. Arid Environ.* **1997**, *37*, 599–608. [CrossRef]
5. Wang, X.M.; Chen, F.H.; Dong, Z.B. The relative role of climatic and human factors in desertification in semiarid China. *Glob. Environ. Chang.* **2006**, *16*, 48–57. [CrossRef]
6. Yang, X.; Zhang, K.; Jia, B.; Ci, L. Desertification assessment in China: An overview. *J. Arid. Environ.* **2005**, *63*, 517–531. [CrossRef]
7. Wang, T.; Xue, X.; Zhou, L.; Guo, J. Combating aeolian desertification in northern China. *Land Degrad. Dev.* **2015**, *26*, 118–132. [CrossRef]
8. Zhou, W.; Gang, C.; Zhou, F.; Li, J.; Dong, X.; Zhao, C. Quantitative assessment of the individual contribution of climate and human factors to desertification in northwest China using net primary productivity as an indicator. *Ecol. Indic.* **2015**, *48*, 560–569. [CrossRef]
9. Xu, D.; Li, C.; Song, X.; Ren, H. The dynamics of desertification in the farming-pastoral region of north China over the past 10 years and their relationship to climate change and human activity. *Catena* **2014**, *123*, 11–22. [CrossRef]
10. Hostert, P.; Roder, A.; Jarmer, T.; Udelhoven, T.; Hill, J. The potential of remote sensing and GIS for desertification monitoring and assessment. *Ann. Arid Zone* **2001**, *40*, 103–140.
11. Hellden, U.; Tottrup, C. Regional desertification: A global synthesis. *Glob. Planet. Chang.* **2008**, *64*, 169–176. [CrossRef]
12. Wang, T.; Yan, C.Z.; Song, X.; Xie, J.L. Monitoring recent trends in the area of aeolian desertified land using Landsat images in China's Xinjiang region. *ISPRS J. Photogramm.* **2012**, *68*, 184–190. [CrossRef]
13. Collado, A.D.; Chuvieco, E.; Camarasa, A. Satellite remote sensing analysis to monitor desertification processes in the crop-rangeland boundary of Argentina. *J. Arid Environ.* **2002**, *52*, 121–133. [CrossRef]
14. Liberti, M.; Simoniello, T.; Carone, M.T.; Coppola, R.; D'Emilio, M.; Macchiato, M. Mapping badland areas using Landsat TM/ETM satellite imagery and morphological data. *Geomorphology* **2009**, *106*, 333–343. [CrossRef]
15. Li, J.; Yang, X.; Jin, Y.; Yang, Z.; Huang, W.; Zhao, L.; Gao, T.; Yu, H.; Ma, H.; Qin, Z.; et al. Monitoring and analysis of grassland desertification dynamics using Landsat images in Ningxia, China. *Remote Sens. Environ.* **2013**, *138*, 19–26. [CrossRef]
16. Holm, A.M.; Cridland, S.W.; Roderick, M.L. The use of time-integrated NOAA NDVI data and rainfall to assess landscape degradation in the arid shrubland of Western Australia. *Remote Sens. Environ.* **2003**, *85*, 145–158. [CrossRef]

17. Geerken, R.; Ilaiwi, M. Assessment of rangeland degradation and development of a strategy for rehabilitation. *Remote Sens. Environ.* **2004**, *90*, 490–504. [CrossRef]
18. Tollefson, J.; Gilbert, N. Rio report card. *Nature* **2012**, *486*, 20–23. [CrossRef] [PubMed]
19. Cudahy, T.; Caccetta, M.; Thomas, M.; Hewson, R.; Abrams, M.; Kato, M.; Kashimura, O.; Ninomiya, Y.; Yamaguchi, Y.; Collings, S.; et al. Satellite-derived mineral mapping and monitoring of weathering, deposition and erosion. *Sci. Rep.* **2016**, *6*, 23702. [CrossRef] [PubMed]
20. Wessels, K.J.; van den Bergh, F.; Scholes, R.J. Limits to detectability of land degradation by trend analysis of vegetation index data. *Remote Sens. Environ.* **2012**, *125*, 10–22. [CrossRef]
21. Becerril-Pina, R.; Mastachi-Loza, C.A.; Gonzalez-Sosa, E.; Diaz-Delgado, C.; Ba, K.M. Assessing desertification risk in the semi-arid highlands of central Mexico. *J. Arid Environ.* **2015**, *120*, 4–13. [CrossRef]
22. Xiao, J.; Shen, Y.; Tateishi, R.; Bayaer, W. Development of topsoil grain size index for monitoring desertification in arid land using remote sensing. *Int. J. Remote Sens.* **2006**, *27*, 2411–2422. [CrossRef]
23. Lamchin, M.; Lee, J.Y.; Lee, W.K.; Lee, E.J.; Kim, M.; Lim, C.H.; Choi, H.A.; Kim, S.R. Assessment of land cover change and desertification using remote sensing technology in a local region of Mongolia. *Adv. Space Res.* **2016**, *57*, 64–77. [CrossRef]
24. Rasmussen, K.; Fog, B.; Madsen, J.E. Desertification in reverse? Observations from northern Burkina Faso. *Glob. Environ. Chang.* **2001**, *11*, 271–282.
25. Khire, M.V.; Agarwadkar, Y.Y. Qualitative analysis of extent and severity of desertification for semi-arid regions using remote sensing techniques. *Int. J. Environ. Sci. Dev.* **2014**, *5*, 238–243. [CrossRef]
26. Xu, E.Q.; Zhang, H.Q.; Li, M.X. Object-based mapping of karst rocky desertification using a support vector machine. *Land Degrad. Dev.* **2015**, *26*, 158–167. [CrossRef]
27. Prince, S.D.; Becker-Reshef, I.; Rishmawi, K. Detection and mapping of long-term land degradation using local net production scaling: Application to Zimbabwe. *Remote Sens. Environ.* **2009**, *113*, 1046–1057. [CrossRef]
28. Wang, X.; Chen, F.; Hasi, E.; Li, J. Desertification in China: An assessment. *Earth Sci. Rev.* **2008**, *88*, 188–206. [CrossRef]
29. Zheng, Y.R.; Xie, Z.X.; Robert, C.; Jiang, L.H.; Shimizu, H. Did climate drive ecosystem change and induce desertification in Otindag sandy land, China over the past 40 years? *J. Arid Environ.* **2006**, *64*, 523–541. [CrossRef]
30. Ma, H.; Lv, Y.; Li, H.X. Complexity of ecological restoration in China. *Ecol. Eng.* **2013**, *52*, 75–78. [CrossRef]
31. Feng, Q.; Ma, H.; Jiang, X.; Wang, X.; Cao, S. What has caused desertification in China? *Sci. Rep.* **2015**, *5*, 15998. [CrossRef] [PubMed]
32. Evans, J.; Geerken, R. Discrimination between climate and human-induced dryland degradation. *J. Arid Environ.* **2004**, *57*, 535–554. [CrossRef]
33. Wessels, K.J.; Prince, S.D.; Malherbe, J.; Small, J.; Frost, P.E.; VanZyl, D. Can human-induced land degradation be distinguished from the effects of rainfall variability? A case study in South Africa. *J. Arid Environ.* **2007**, *68*, 271–297.
34. Prince, S.D.; Wessels, K.J.; Tucker, C.J.; Nicholson, S.E. Desertification in the Sahel: A reinterpretation of a reinterpretation. *Glob. Chang. Biol.* **2007**, *13*, 1308–1313. [CrossRef]
35. Wessels, K.J.; Prince, S.D.; Frost, P.E.; van Zyl, D. Assessing the effects of human-induced land degradation in the former homelands of northern South Africa with a 1 km AVHRR NDVI time-series. *Remote Sens. Environ.* **2004**, *91*, 47–67. [CrossRef]
36. Haberl, H.; Krausmann, F.; Erb, K.H.; Schulz, N.B. Human appropriation of net primary production. *Science* **2002**, *296*, 1968–1969. [CrossRef] [PubMed]
37. Rojstaczer, S.; Sterling, S.M.; Moore, N.J. Human appropriation of photosynthesis products. *Science* **2001**, *294*, 2549–2552. [CrossRef] [PubMed]
38. Krausmann, F.; Erb, K.H.; Gingrich, S.; Haberl, H.; Bondeau, A.; Gaube, V.; Lauk, C.; Plutzar, C.; Searchinger, T.D. Global human appropriation of net primary production doubled in the 20th century. *Proc. Natl. Acad. Sci. USA* **2013**, *110*, 10324–10329. [CrossRef] [PubMed]
39. Haberl, H.; Erb, K.H.; Krausmann, F.; Gaube, V.; Bondeau, A.; Plutzar, C.; Gingrich, S.; Lucht, W.; Fischer-Kowalski, M. Quantifying and mapping the human appropriation of net primary production in earth's terrestrial ecosystems. *Proc. Natl. Acad. Sci. USA* **2007**, *104*, 12942–12947. [CrossRef] [PubMed]

40. Wessels, K.J.; Prince, S.D.; Reshef, I. Mapping land degradation by comparison of vegetation production to spatially derived estimates of potential production. *J. Arid Environ.* **2008**, *72*, 1940–1949. [CrossRef]
41. Liu, L.Y.; Skidmore, E.; Hasi, E.; Wagner, L.; Tatarko, J. Dune sand transport as influenced by wind directions, speed and frequencies in the Ordos Plateau, China. *Geomorphology* **2005**, *67*, 283–297. [CrossRef]
42. Roy, D.P.; Zhang, H.K.; Ju, J.; Gomez-Dans, J.L.; Lewis, P.E.; Schaaf, C.B.; Sun, Q.; Li, J.; Huang, H.; Kovalskyy, V. A general method to normalize Landsat reflectance data to nadir BRDF adjusted reflectance. *Remote Sens. Environ.* **2016**, *176*, 255–271. [CrossRef]
43. Lee, D.S.; Storey, J.C.; Choate, M.J.; Hayes, R.W. Four years of Landsat-7 on-orbit geometric calibration and performance. *IEEE Trans. Geosci. Remote Sens.* **2004**, *42*, 2786–2795. [CrossRef]
44. Roy, D.P.; Wulder, M.A.; Loveland, T.R.; Woodcoc, C.E.; Allen, R.G.; Anderson, M.C.; Helder, D.; Irons, J.R.; Johnson, D.M.; Kennedy, R.; et al. Landsat-8: Science and product vision for terrestrial global change research. *Remote Sens. Environ.* **2014**, *145*, 154–172. [CrossRef]
45. Chander, G.; Markham, B.L.; Helder, D.L. Summary of current radiometric calibration coefficients for Landsat MSS, TM, ETM+, and EO-1 ALI sensors. *Remote Sens. Environ.* **2009**, *113*, 893–903. [CrossRef]
46. Qi, J.; Chehbouni, A.; Huete, A.R.; Kerr, Y.H.; Sorooshian, S. A modified soil adjusted vegetation index. *Remote Sens. Environ.* **1994**, *48*, 119–126. [CrossRef]
47. Rikimaru, A.; Roy, P.; Miyatake, S. Tropical forest cover density mapping. *Trop. Ecol.* **2002**, *43*, 39–47.
48. Liang, S.L. Narrowband to broadband conversions of land surface albedo I algorithms. *Remote Sens. Environ.* **2001**, *76*, 213–238. [CrossRef]
49. Wang, Y.; Yan, X. Climate change induced by southern hemisphere desertification. *Phys. Chem. Earth* **2016**. [CrossRef]
50. Robinove, C.J.; Chavez, P.S.; Gehring, D.; Holmgren, R. Arid land monitoring using Landsat albedo difference images. *Remote Sens. Environ.* **1981**, *11*, 133–156. [CrossRef]
51. Wang, T.; Wu, W.; Xue, X.; Sun, Q.W.; Chen, G.T. Study of spatial distribution of sandy desertification in north China in recent 10 years. *Sci. China Ser. D* **2004**, *47*, 78–88. [CrossRef]
52. Sun, C.; Liu, Y.; Zhao, S.; Zhou, M.; Yang, Y.; Li, F. Classification mapping and species identification of salt marshes based on a short-time interval NDVI time-series from HJ-1 optical imagery. *Int. J. Appl. Earth Obs.* **2016**, *45*, 27–41. [CrossRef]
53. Friedl, M.A.; Brodley, C.E.; Strahler, A.H. Maximizing land cover classification accuracies produced by decision trees at continental to global scales. *IEEE Trans. Geosci. Remote. Sens.* **1999**, *37*, 969–977. [CrossRef]
54. Quinlan, J.R. Simplifying decision trees. *Int. J. Hum. Comput. Stud.* **1999**, *51*, 497–510. [CrossRef]
55. Mingers, J. An empirical comparison of pruning methods for decision tree induction. *Mach. Learn.* **1989**, *4*, 227–243. [CrossRef]
56. Potter, C.S.; Randerson, J.T.; Field, C.B.; Matson, P.A.; Vitousek, P.M.; Mooney, H.A.; Klooster, S.A. Terrestrial ecosystem production—A process model-based on global satellite and surface data. *Glob. Biogeochem. Cycles* **1993**, *7*, 811–841. [CrossRef]
57. Field, C.B.; Randerson, J.T.; Malmstrom, C.M. Global net primary production—Combining ecology and remote-sensing. *Remote Sens. Environ.* **1995**, *51*, 74–88. [CrossRef]
58. Wu, Z.; Wu, J.; Liu, J.; He, B.; Lei, T.; Wang, Q. Increasing terrestrial vegetation activity of ecological restoration program in the Beijing–Tianjin sand source region of China. *Ecol. Eng.* **2013**, *52*, 37–50. [CrossRef]
59. Zhu, W.Q.; Pan, Y.Z.; He, H.; Yu, D.Y.; Hu, H.B. Simulation of maximum light use efficiency for some typical vegetation types in China. *Chin. Sci. Bull.* **2006**, *51*, 457–463. [CrossRef]
60. Yu, D.Y.; Shi, P.J.; Han, G.Y.; Zhu, W.Q.; Du, S.Q.; Xun, B. Forest ecosystem restoration due to a national conservation plan in China. *Ecol. Eng.* **2011**, *37*, 1387–1397. [CrossRef]
61. Zhao, M.; Heinsch, F.A.; Nemani, R.R.; Running, S.W. Improvements of the modis terrestrial gross and net primary production global data set. *Remote Sens. Environ.* **2005**, *95*, 164–176. [CrossRef]
62. Pan, S.F.; Tian, H.Q.; Dangal, S.R.S.; Ouyang, Z.Y.; Tao, B.; Ren, W.; Lu, C.Q.; Running, S. Modeling and monitoring terrestrial primary production in a changing global environment: Toward a multiscale synthesis of observation and simulation. *Adv. Meteorol.* **2014**, *2014*, 965936. [CrossRef]
63. Zhang, Y.Q.; Yu, Q.; Jiang, J.; Tang, Y.H. Calibration of Terra/Modis gross primary production over an irrigated cropland on the North China Plain and an alpine meadow on the Tibetan Plateau. *Glob. Chang. Biol.* **2008**, *14*, 757–767. [CrossRef]

64. Lieth, H.; Box, E. Evapotranspiration and primary productivity: C.W. Thornthwaite memorial model. *Publ. Climatol.* **1972**, *25*, 37–46.
65. Piao, S.; Ciais, P.; Huang, Y.; Shen, Z.; Peng, S.; Li, J.; Zhou, L.; Liu, H.; Ma, Y.; Ding, Y.; et al. The impacts of climate change on water resources and agriculture in China. *Nature* **2010**, *467*, 43–51. [CrossRef] [PubMed]
66. Li, B.; Chen, Y.; Chen, Z.; Xiong, H.; Lian, L. Why does precipitation in northwest China show a significant increasing trend from 1960 to 2010? *Atmos. Res.* **2016**, *167*, 275–284. [CrossRef]
67. Dewan, A.M.; Yamaguchi, Y. Land use and land cover change in Greater Dhaka, Bangladesh: Using remote sensing to promote sustainable urbanization. *Appl. Geogr.* **2009**, *29*, 390–401. [CrossRef]
68. Moomen, A.-W.; Dewan, A.; Corner, R. Landscape assessment for sustainable resettlement of potentially displaced communities in Ghana's emerging northwest gold province. *J. Clean. Prod.* **2016**, *133*, 701–711. [CrossRef]
69. Li, N.; Yan, C.Z.; Xie, J.L. Remote sensing monitoring recent rapid increase of coal mining activity of an important energy base in northern China, a case study of Mu Us sandy land. *Resour. Conserv. Recycl.* **2015**, *94*, 129–135. [CrossRef]